



Chinese Pharmaceutical Association  
Institute of Materia Medica, Chinese Academy of Medical Sciences

Acta Pharmaceutica Sinica B

[www.elsevier.com/locate/apsb](http://www.elsevier.com/locate/apsb)  
[www.sciencedirect.com](http://www.sciencedirect.com)



ORIGINAL ARTICLE

# Converting bacteria into autologous tumor vaccine *via* surface biomineralization of calcium carbonate for enhanced immunotherapy

Lina Guo<sup>a</sup>, Jinsong Ding<sup>a</sup>, Wenhui Zhou<sup>a,b,\*</sup>

<sup>a</sup>Xiangya School of Pharmaceutical Sciences, Central South University, Changsha 410013, China

<sup>b</sup>Key Laboratory of Biological Nanotechnology of National Health Commission, Xiangya Hospital, Changsha 410008, China

Received 23 March 2023; received in revised form 21 May 2023; accepted 18 June 2023



## KEY WORDS

Bacteria-mediated cancer therapy;  
Tumor microenvironment;  
Calcium carbonate;  
Mineralization;  
Metalloimmunology;  
Autologous tumor vaccine;  
Immunotherapy;  
Tumor metastasis

**Abstract** Autologous cancer vaccine that stimulates tumor-specific immune responses for personalized immunotherapy holds great potential for tumor therapy. However, its efficacy is still suboptimal due to the immunosuppressive tumor microenvironment (ITM). Here, we report a new type of bacteria-based autologous cancer vaccine by employing calcium carbonate (CaCO<sub>3</sub>) biomineralized *Salmonella* (*Sal*) as an *in-situ* cancer vaccine producer and systematical ITM regulator. CaCO<sub>3</sub> can be facilely coated on the *Sal* surface with calcium ionophore A23187 co-loading, and such biomineralization did not affect the bioactivities of the bacteria. Upon intratumoral accumulation, the CaCO<sub>3</sub> shell was decomposed at an acidic microenvironment to attenuate tumor acidity, accompanied by the release of *Sal* and Ca<sup>2+</sup>/A23187. Specifically, *Sal* served as a cancer vaccine producer by inducing cancer cells' immunogenic cell death (ICD) and promoting the gap junction formation between tumor cells and dendritic cells (DCs) to promote antigen presentation. Ca<sup>2+</sup>, on the other hand, was internalized into various types of immune cells with the aid of A23187 and synergized with *Sal* to systematically regulate the immune system, including DCs maturation, macrophages polarization, and T cells activation. As a result, such bio-vaccine achieved remarkable efficacy against both primary and metastatic tumors by eliciting potent anti-tumor immunity with full biocompatibility. This work demonstrated the potential of bioengineered bacteria as bio-active vaccines for enhanced tumor immunotherapy.

© 2023 Chinese Pharmaceutical Association and Institute of Materia Medica, Chinese Academy of Medical Sciences. Production and hosting by Elsevier B.V. This is an open access article under the CC BY-NC-ND license (<http://creativecommons.org/licenses/by-nc-nd/4.0/>).

\*Corresponding author.

E-mail address: [zhouwenhuyaoji@163.com](mailto:zhouwenhuyaoji@163.com) (Wenhui Zhou).

Peer review under the responsibility of Chinese Pharmaceutical Association and Institute of Materia Medica, Chinese Academy of Medical Sciences.

<https://doi.org/10.1016/j.apsb.2023.08.028>

2211-3835 © 2023 Chinese Pharmaceutical Association and Institute of Materia Medica, Chinese Academy of Medical Sciences. Production and hosting by Elsevier B.V. This is an open access article under the CC BY-NC-ND license (<http://creativecommons.org/licenses/by-nc-nd/4.0/>).

## 1. Introduction

Immunotherapy that harnesses the host immune system to kill cancer cells is a promising tumor therapy modality. It has experienced explosive development over the past decades, and various types of immunotherapies have been developed currently, mainly including immune checkpoint inhibitors (ICIs), chimeric antigen receptor T cell therapy (CAR-T), and cancer vaccine treatment<sup>1</sup>. However, while immunotherapy has shown great clinical outcomes in a proportion of patients with complete tumor regression and long-term benefits, the overall therapeutic efficacy is still unsatisfactory, and the response rate remains very low. Moreover, significant side-effects are noticed<sup>2</sup>. For example, ICIs usually cause over-activation of the immune system with dermatologic, gastrointestinal, or rheumatologic toxicity, while CAR-T even leads to organ failure and nervous system damage due to the excessive release of cytokines and neurotoxicity. For comparison, cancer vaccine exerts therapeutic effects by arousing tumor-specific immunostimulation with fewer side effects, which has been proven as a promising approach to not only eradicate the local tumor and metastatic lesions but also prevent tumor rechallenge by establishing long-lasting anti-tumor memory<sup>3–5</sup>.

Cancer vaccines can generally be divided into two subtypes, the preventive and therapeutic vaccines<sup>6</sup>. Despite significant efforts and progresses, the cancer vaccine is still in the stage of cancer prophylaxis, while the development of therapeutic vaccines remains a huge challenge. Basically, therapeutic cancer vaccine functions by delivering tumor cell-specific antigens to stimulate anti-tumor immunity, which mainly requires a few sequential steps for effective tumor therapy, *e.g.*, tumor antigens exposure, antigen presentation, and activation of T cells-based cellular immune responses to eliminate tumor<sup>7,8</sup>. However, it is rather difficult to evoke robust immune responses in cancerous patients by cancer vaccines, and there are several main obstacles to hinder their clinical translation, including inefficient delivery, weak immunogenicity, and low patient relevance of the vaccines, as well as the immunosuppressive tumor microenvironment (ITM) to inhibit cellular immune responses<sup>9–12</sup>. Therefore, it is highly desirable to develop a therapeutic vaccine that can simultaneously achieve high delivery efficiency, strong immunogenicity with personalized patient specificity, and systematic ITM regulation.

To meet the above-mentioned demand, autologous tumor cell-based vaccines have been developed, which display better efficacy than traditional cancer vaccines by eliciting robust anti-tumor immune responses for personalized immunotherapy<sup>13</sup>. Autologous cancer vaccines can either be generated by *in vitro* preparation or *in-situ* production in tumor tissue. *In vitro* preparation of autologous vaccines usually requires highly trained personnel and complex preparation procedures, thus with high treatment costs. In addition, such a strategy also encounters the problems of low preparation yield, delayed dosing schedule, unpredicted low effectiveness, and unsatisfactory efficacy<sup>11,13</sup>. As such, *in vivo* vaccine generation is compared to be a better choice given its simple application process, which has attracted great research attention recently<sup>11,12</sup>. The basic rationale of *in vivo* vaccine generation is to transform tumors into an *in-situ* vaccine, which in turn induces an anti-tumor immunity<sup>14</sup>. For example, our group and many other groups employed chemotherapy, radiotherapy, and phototherapies to damage tumor cells that undergo immunogenic cell death (ICD), through which dying cancer cells could release abundant and personalized tumor antigens<sup>10,11,15–17</sup>. While these methods are straightforward with the advantages of simplicity, the

use of auxiliary treatments would bring additional side effects to patients. Moreover, the exposure of tumor antigens alone fails to elicit an adequate infiltration and activation of cytotoxic T lymphocytes (CTLs) in tumor stroma because of ITM<sup>18</sup>. Therefore, feasible approaches that can amplify the immune responses are highly desired to enhance autologous tumor cell-based vaccines for cancer immunotherapy.

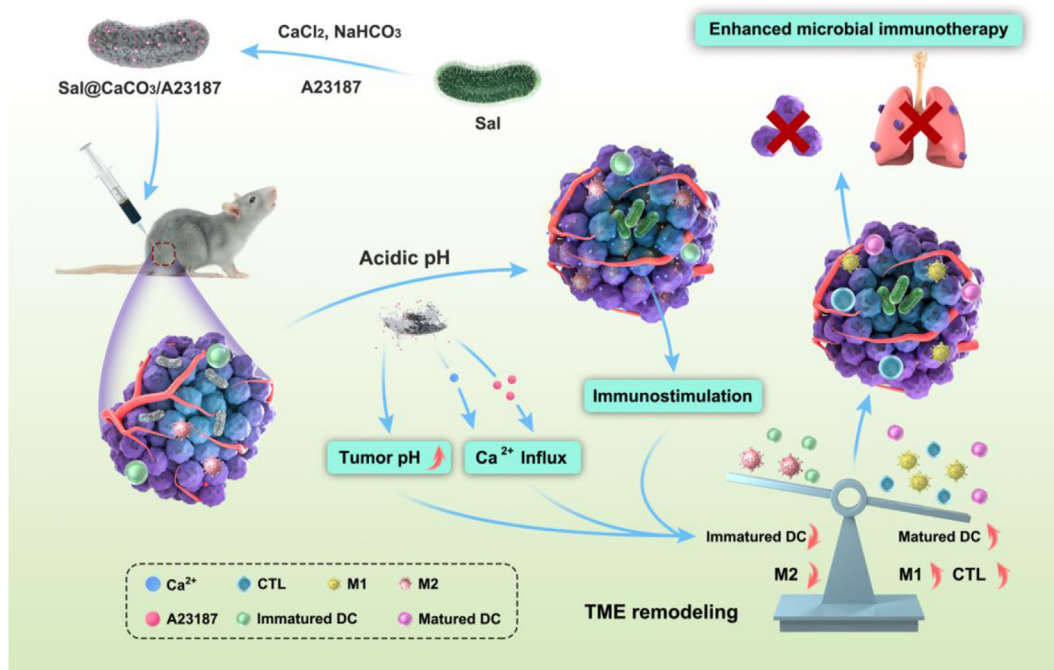
In this work, we employed *Salmonella* (*Sal*) as a tool to simultaneously produce *in-situ* tumor vaccines and regulate ITM. *Sal* has been widely used in bacteria-based cancer therapy owing to its excellent tumor targetability, intrinsic tumoricidal activity, and fully sequenced genomes for convenient genetic manipulation, which has entered clinical trials<sup>19–24</sup>. It could directly induce tumor cells ICD to expose tumor antigens<sup>25,26</sup>, and regulate ITM from multiple dimensions<sup>19,27–31</sup>. In this regard, *Sal* can be used as an *in-situ* tumor vaccine with self-reproduction capability. Encouraged by excellent efficacy in preclinical studies, some strains have advanced to clinical trials in the early of this century<sup>32</sup>. However, the clinical results were somehow frustrated, with no objective tumor regression being observed<sup>33,34</sup>. Several reasons can explain such failure, including rapid clearance of bacteria by the immune system upon intravenous injection<sup>35–38</sup>, as well as strict restriction of bacteria at the central necrotic zone of the tumor by neutrophils to limit their efficacy<sup>39,40</sup>.

To improve the therapeutic outcomes of bacteria-based cancer vaccines, here we designed a calcium carbonate (CaCO<sub>3</sub>) bio-mineralized *Sal* as an autologous tumor vaccine with capabilities to systematically regulate ITM for enhanced immunotherapy (Scheme 1). Through a facile mineralization process, *Sal* was coated with a biocompatible and biodegradable CaCO<sub>3</sub> shell to form *Sal*@CaCO<sub>3</sub>. Interestingly, such mineralization did not affect the activity and functions of *Sal*, and upon accumulation at the acidic tumor microenvironment, the CaCO<sub>3</sub> shell could be exfoliated by virtue of its pH-responsive degradation<sup>41</sup>, allowing the release of *Sal* and Ca<sup>2+</sup> to exert their respective functions. Specifically, *Sal* could not only induce tumor cells ICD to release tumor antigens but also facilitate crosstalk between tumor cells and DCs *via* the formation of gap junction to promote antigen presentation and DCs maturation, which translates the tumor tissue into antigen depots. The release of Ca<sup>2+</sup>, on the other hand, served as a second messenger to systematically regulate ITM<sup>42</sup>. To promote the intracellular delivery of Ca<sup>2+</sup>, the calcium ionophore A23187 was co-loaded on the surface of *Sal*@CaCO<sub>3</sub> to form *Sal*@CaCO<sub>3</sub>/A23187. A23187 could form lipid-soluble complexes with Ca<sup>2+</sup>, transport Ca<sup>2+</sup> out of intracellular stores into the cytosol, and induce store-operated Ca<sup>2+</sup> entry by opening the calcium channels across the cell membrane<sup>43</sup>. With the co-delivery of A23187, significant Ca<sup>2+</sup> influx was observed, leading to M1 polarization of macrophages, DCs maturation, and T cells activation, all of which could synergize with *Sal* for better immunotherapy. As a result, a potent anti-tumor effect was achieved against both primary and metastatic tumors with full biocompatibility.

## 2. Materials and methods

### 2.1. Materials

The anhydrous calcium chloride (C832203) was purchased from Macklin Co., Ltd. (Shanghai, China). The sodium bicarbonate (10018960) was bought from Sinopharm Chemical Reagent Co.,



**Scheme 1** Schematic illustration of the construction of *Sal*@CaCO<sub>3</sub>/A23187 for enhanced immunotherapy.

Ltd. (Shanghai, China). The calcium ionophore A23187 (MZ2153) and SYTO 9/PI Live/Dead Bacterial Double Stain Kit (MX4234) were purchased from Maokang Biotechnology Co., Ltd. (Shanghai, China). The Roswell Park Memorial Institute (RPMI)-1640 medium (11875-093), Dulbecco's modified Eagle's medium (DMEM, 10569-010), fetal bovine serum (FBS, 10100-147) and penicillin-streptomycin solution (15070-063) were purchased from Gibco Life Technologies, Inc. (Grand Island, USA). The calcium ion fluorescent probe Fluo-8 AM assay kit (C0012) was bought from Appligen Technologies (Beijing, China). Calcium Chromogenic Kit (S1063S) and Calcein-AM (C2012) were obtained from Beyotime Biotechnology (Shanghai, China). The DDAO (HY-114879) and D-luciferin potassium salt (HY-12591B) were bought from MedChemExpress (New Jersey, USA). The fluorescence-labeled antibody against CD11c (17-0114-81), F4/80 (12-4801-82), CD80 (11-0801-82), CD86 (12-0862-82), CD206 (MA5-16870), MHC II (11-5321-82), CD3 (11-0032-82), CD4 (17-0042-82) and CD8 (12-0081-82) were obtained from eBioscience (California, USA). The FITC-labelled antibody against CRT (bs-5913R) was bought from Bioss (Beijing, China). The ELISA kits for HMGB1 (MM-44107M1), TNF- $\alpha$  (MM-0132M1), IFN- $\gamma$  (MM-0182M1, MM-0033H1), IL-2 (MM-0055H1), IL-6 (MM-0163M1) and IL-10 (MM-0176M1) were purchased from Meimian Industrial Co., Ltd. (Yancheng, China). The luciferin-based ATP assay kit (S0026) was bought from Beyotime Biotechnology (Shanghai, China). The LB broth (L8291), 4',6-diamidino-2-phenylindole (DAPI, C0065), Mouse Peripheral Blood Neutrophil Isolation Kit (P9201), and Cell Apoptosis Detection Kit (CA1040) were obtained from Solarbio Biotech Co., Ltd. (Beijing, China). The LB agar powder (A507003) and gentamicin (A506614) were purchased from Sangon Biotech Co., Ltd. (Shanghai, China). The primary antibody against connexin 43 (Cx43, 26980-1-AP), CD80 (66406-1-Ig), CD86 (13395-1-AP), and CD206 (18704-1-AP) were bought from Proteintech Group (Chicago, USA). The primary antibodies

against CD4 (A0362) and CD8A (A11856) were obtained from ABclonal (Wuhan, China). The assay kits for alanine transaminase (ALT, C009-2-1), aspartate transaminase (AST, C010-2-1), blood urea nitrogen (BUN, C013-2-1), and creatinine (Cre, C011-2-1) were purchased from Jiancheng Bioengineering Institute (Nanjing, China). The aPD-L1 (BE0361) was obtained from BioXcell (New Hampshire, USA).

## 2.2. Bacteria and cell culture

The *Salmonella typhimurium* strain  $\Delta$ ppGpp (denoted as *Sal*) was kindly provided by Jinhai Zheng from Hunan University. The bacteria were cultured in LB broth and placed in a shaking incubator at 37 °C and 180 rpm. Then, the cultures were centrifuged at 3000 rpm for 5 min (TGL20M, Yingtai, Changsha, China). The collected bacteria were resuspended in sterile saline for further use.

The murine melanoma cells (B16F10), murine bone marrow-derived dendritic cells (DC2.4), murine macrophage cells (RAW264.7), and human acute leukemia T lymphocytes (Jurkat T cells) were obtained from Xiangya cell center (Changsha, China). The luciferase-tagged B16F10 cells (B16F10-luc) were kindly provided by Prof. Xiang Chen from Xiangya Hospital of Central South University. The B16F10 cells were cultured in DMEM medium, while the others were cultured in RPMI-1640 medium, with 10% FBS and 1% penicillin-streptomycin solution supplemented and cultured at 37 °C with 5% CO<sub>2</sub>. The puromycin (1.5  $\mu$ g/mL) was also supplemented for the B16F10-luc cells.

## 2.3. Preparation and characterizations of *Sal*@CaCO<sub>3</sub>/A23187

### 2.3.1. Preparation and characterizations of *Sal*@CaCO<sub>3</sub>

The concentration of bacteria suspensions was adjusted to  $2.9 \times 10^7$  CFU/mL according to the optical density (OD) values at 600 nm. Then, 0.2 mL of CaCl<sub>2</sub> (1 mol/L) and 0.05 mL of

NaHCO<sub>3</sub> (1 mol/L) were successively added to 1.75 mL of bacteria suspensions, followed by stirring at room temperature for 5 min. The Sal@CaCO<sub>3</sub> was collected by centrifugation at 3000 rpm for 5 min (TGL20M, Yingtai, Changsha, China). The size of Sal@CaCO<sub>3</sub> was measured by the Malvern Zeta Sizer Nano series (ZS-90, Malvern Instruments, Great Malvern, UK). The morphology and element mapping were observed by transmission electron microscope (TEM) (Titan G2 60–300, FEI, Hillsboro, USA). Fourier transform infrared (FT-IR) spectrometer (AVATAR360, Nicolet, Wisconsin, USA) was used to scan FT-IR spectra.

### 2.3.2. Preparation and characterizations of Sal@CaCO<sub>3</sub>/A23187

Briefly, 65 µL of A23187 stock solution dissolved in DMSO (1.9 mmol/L) was added to 935 µL water and then sonicated for 5 min to obtain A23187 NPs. The Sal@CaCO<sub>3</sub> was resuspended and incubated with A23187 NPs (100 µM) at 37 °C for 2 h. The Sal@CaCO<sub>3</sub>/A23187 was also collected by centrifugation at 3000 rpm for 5 min (TGL20M, Yingtai, Changsha, China). The Sal, Sal@CaCO<sub>3</sub>, and Sal@CaCO<sub>3</sub>/A23187 were imaged under ultraviolet light and a fluorescent microscope to demonstrate the successful loading. The fluorescence intensity of A23187 (Ex: 378 nm, Em: 439 nm) in the precipitate was measured by a fluorescence spectrophotometer (F-2700, Hitachi, Tokyo, Japan) after dissolving with DMSO to obtain the adsorbing capacity.

### 2.4. Bacterial viability

The bacterial viability of Sal, Sal@CaCO<sub>3</sub>, and Sal@CaCO<sub>3</sub>/A23187 was investigated by plate coating and SYTO 9/PI double staining. For the plate coating, Sal, Sal@CaCO<sub>3</sub>, and Sal@CaCO<sub>3</sub>/A23187 were plated on solid LB agar plates post 1000-fold dilution and cultured at 37 °C. The bacterial colonies on the plates were observed and counted after 24 h incubation. For SYTO 9/PI double staining, Sal, Sal@CaCO<sub>3</sub>, and Sal@CaCO<sub>3</sub>/A23187 were collected by centrifugation and resuspended in saline. Then, 1.5 µL of both SYTO 9 and PI were added into 1 mL of bacterial suspensions and incubated in the dark for 15 min, followed by washing with saline three times. The samples were imaged using a fluorescent microscope (ECLIPSE Ti-S, Nikon, Tokyo, Japan).

### 2.5. Bacterial growth curve

The Sal, Sal@CaCO<sub>3</sub>, and Sal@CaCO<sub>3</sub>/A23187 were collected, seeded in a 96-well plate with LB broth, and then cultured in a microplate reader (Infinite M200 PRO, TECAN, Grödig, Austria) at 37 °C and constant shaking. The bacterial growth curves were drawn according to the OD values at 600 nm recorded every hour.

### 2.6. Acidity neutralization effect

Sal or Sal@CaCO<sub>3</sub> was immersed in PBS (10 mmol/L, pH 6.5) with constant stirring. The pH values were recorded within 30 min by a pH meter (PHSJ-4F, INESA, Shanghai, China).

### 2.7. Ca<sup>2+</sup>/A23187 release

The Sal@CaCO<sub>3</sub>/A23187 was dispersed in the buffer of different pH (7.4/6.5) and shaken at 100 rpm and 37 °C in a shaking

incubator. The samples were withdrawn at predetermined time points (0, 0.5, 1, 2, 4, 8, 12, 24, and 48 h) and centrifuged at 3000 rpm for 5 min (TGL20M, Yingtai, Changsha, China). The amount of Ca<sup>2+</sup> and A23187 in the supernatant was determined by Calcium Chromogenic Kit and fluorescence intensity quantification (Ex: 378 nm, Em: 439 nm), respectively.

### 2.8. Cell viability study

The RAW264.7 or DC2.4 cells were seeded in 96-well plates at a density of 5 × 10<sup>3</sup> cells per well and incubated overnight. Then, different concentrations of A23187 (1, 2, 5, 10, 20, and 50 µmol/L) were added. After incubating for 24 h, the medium was replaced by MTT (0.5 mg/mL) and further incubated for 4 h. Then, the medium was discarded, and 100 µL of DMSO was added to dissolve the generated formazan. The absorbance at 490 nm was measured by a microplate reader (TECAN).

### 2.9. Intracellular Ca<sup>2+</sup> detection

The RAW264.7 cells were seeded in confocal dishes at a density of 5 × 10<sup>4</sup> cells per dish and incubated overnight. After pre-treating with A23187 (5 µmol/L) for 11 h, the cells were treated with Ca<sup>2+</sup> (5 mmol/L) for 1 h. Afterward, Fluo-8 AM (5 µmol/L) was added for 1 h incubation to stain the cells, followed by washing with PBS three times. The cells were collected and analyzed by flow cytometry (CytoFLEX, Beckman Coulter, Suzhou, China). For fluorescence imaging, the cells were fixed with 4% paraformaldehyde for 10 min, the cell nuclei were stained with DAPI (1 µg/mL) for 10 min, and then they were imaged with confocal laser scanning microscopy (CLSM) (LSM 900, Zeiss, Oberkochen, Germany).

### 2.10. Ca<sup>2+</sup>-Mediated immune activation

For DCs maturation, DC2.4 cells were seeded in 24-well plates and incubated overnight. After pretreating with A23187 (5 µmol/L) for 11 h, the cells were treated with Ca<sup>2+</sup> (5 mmol/L) for 1 h, followed by replacement with the fresh cell culturing medium. The B16F10 cell lysates obtained from repeated freezing and thawing were added and further incubated for 16 h. The cells were collected and incubated with anti-MHC II-FITC and anti-CD86-PE at 4 °C for 1 h. The samples were analyzed by flow cytometry (Beckman Coulter), and MHC II and CD86 double-positive cells were quantified.

For macrophage polarization, RAW264.7 cells were seeded in 24-well plates and incubated overnight. IL-4 (100 ng/mL) was added for 24 h incubation to induce M2 polarization. Afterward, the cells were treated with A23187 (5 µmol/L) for 11 h and then treated with Ca<sup>2+</sup> (5 mmol/L) for 1 h, followed by replacement with the fresh cell culturing medium. After further incubation for 16 h, the cells were collected and incubated with anti-CD80-FITC and anti-CD206-FITC at 4 °C for 1 h. The fluorescence intensity of these samples was measured by flow cytometry (Beckman Coulter).

For T cell activation, Jurkat T cells were seeded in 24-well plates and successively treated with A23187 (5 µmol/L) for 11 h and Ca<sup>2+</sup> (5 mmol/L) for 1 h. Then, the medium was replaced by the fresh cell culturing medium and further incubated for 36 h. After the incubation, the cells were collected by centrifugation, and RIPA lysis buffer was added to extract the total protein, which was quantified by BCA Protein Quantification Kit. The content of

IL-2 and IFN- $\gamma$  in the supernatant was measured by corresponding ELISA kits. The secretion levels were finally expressed as pg/ $\mu$ g protein.

### 2.11. Cell apoptosis detection

The B16F10 cells were seeded in a 6-well plate and incubated overnight. *Sal* or *Sal@CaCO<sub>3</sub>* pretreated in buffer (pH 7.4/6.5) for 0.5 h was added. After incubating for 24 h, the cells were collected and washed with PBS, followed by resuspending in binding buffer (1  $\times$ ). The Annexin-FITC and PI were added to stain the cells, and the samples were measured by flow cytometry (Beckman Coulter).

### 2.12. Immunogenic cell death detection

The B16F10 cells were seeded in 12-well plates and incubated overnight. *Sal* or *Sal@CaCO<sub>3</sub>* pretreated in buffer (pH 7.4/6.5) for 0.5 h was added for 24 h incubation. Afterward, the cells were collected and analyzed by flow cytometry (Beckman Coulter) after incubating with anti-calreticulin (CRT)-FITC at 4  $^{\circ}$ C for 0.5 h. In addition, the supernatant was collected, and the release of high-mobility group box 1 protein (HMGB1) and ATP was determined by kits.

### 2.13. Gap junction formation

#### 2.13.1. Cx43 expression

The Cx43 expression was investigated by Western Blot (WB). Briefly, the B16F10 and DC2.4 cells were seeded in 6-well plates and incubated overnight. *Sal* or *Sal@CaCO<sub>3</sub>* pretreated in buffer (pH 7.4/6.5) for 0.5 h was added for 4 h incubation, followed by washing with PBS three times. Afterward, the complete medium supplemented with gentamicin (50  $\mu$ g/mL) was added for 20 h incubation. Then, RIPA lysis buffer was used to extract the total protein, whose concentration was adjusted to the same according to the BCA quantification results. After denaturation at 95  $^{\circ}$ C for 10 min, the samples were separated by sodium dodecyl sulfate-polyacrylamide gel electrophoresis (SDS-PAGE) and then transferred to the PVDF membrane. The membranes were blocked with 5% non-fat milk for 1 h, incubated with the primary antibodies against Cx43 at 4  $^{\circ}$ C overnight, and then incubated with secondary antibody at room temperature for 1 h. Finally, the membranes were visualized by ECL.

#### 2.13.2. Fluorescent dye transfer

The B16F10 and DC2.4 cells were seeded in 6-well plates and incubated overnight. *Sal* or *Sal@CaCO<sub>3</sub>* pretreated in buffer (pH 7.4/6.5) for 0.5 h was added for 4 h incubation, followed by washing with PBS three times. Afterward, the complete medium supplemented with gentamicin (50  $\mu$ g/mL) was added for 20 h incubation. Then, the B16F10 and DC2.4 cells were collected separately and stained with Calcein-AM and DDAO at 37  $^{\circ}$ C for 30 min, respectively. The stained cells were then co-incubated (B16F10:DC2.4 = 1:2) for 1 h and subjected to flow cytometry (Beckman Coulter) analysis.

### 2.14. Synergistic immune activation by *Sal* and $Ca^{2+}$ influx

For DCs maturation, DC2.4 cells were seeded in 24-well plates and incubated overnight. *Sal*, *Sal@CaCO<sub>3</sub>*, or *Sal@CaCO<sub>3</sub>/A23187* was added for 24 h incubation, with gentamicin (100  $\mu$ g/mL)

supplemented in the cell culturing medium. The cells were collected by centrifugation and incubated with anti-MHC II-FITC and anti-CD86-PE at 4  $^{\circ}$ C for 1 h. The samples were analyzed by flow cytometry (Beckman Coulter), and MHC II and CD86 double-positive cells were quantified.

For macrophage polarization, RAW264.7 cells were seeded in 24-well plates and incubated overnight. IL-4 (100 ng/mL) was added for 24 h incubation to induce M2 polarization. Afterward, the cells were treated with *Sal*, *Sal@CaCO<sub>3</sub>*, or *Sal@CaCO<sub>3</sub>/A23187* for 24 h, with gentamicin (100  $\mu$ g/mL) supplemented in the cell culturing medium. Then, the cells were collected and incubated with anti-CD86-PE and anti-CD206-PE at 4  $^{\circ}$ C for 1 h. The fluorescence intensity of these samples was measured by flow cytometry (Beckman Coulter).

For T cells activation, Jurkat T cells were seeded in 24-well plates and treated with *Sal*, *Sal@CaCO<sub>3</sub>*, or *Sal@CaCO<sub>3</sub>/A23187* for 48 h, with gentamicin (100  $\mu$ g/mL) supplemented in the cell culturing medium. After the incubation, the cells were collected by centrifugation, and RIPA lysis buffer was added to extract the total protein, which was quantified by BCA Protein Quantification Kit. The content of IFN- $\gamma$  in the supernatant was measured by ELISA kits and finally expressed as pg/ $\mu$ g protein.

### 2.15. Animal models

The male C57BL/6 mice (6–8 weeks old) were provided by Hunan SJA Laboratory Animal Co., Ltd. (Changsha, China). All the experimental procedures were executed according to the protocols approved by Central South University Animal Care and Use Committee. For the establishment of melanoma tumor models, the mice were subcutaneously inoculated with suspensions containing  $1 \times 10^6$  B16F10 cells. The tumor volume was calculated from Eq. (1):

$$\text{Tumor volume} = (\text{Length} \times \text{Width}^2)/2 \quad (1)$$

### 2.16. In vivo biodistribution

When the tumor volume reached  $\sim 100 \text{ mm}^3$ , the mice were intratumorally injected with 25  $\mu$ L of *Sal@CaCO<sub>3</sub>/A23187* at a *Sal* dose of  $5 \times 10^6$  CFU per mouse. The tumors and major organs, including the heart, liver, spleen, lung, and kidneys, were collected on Days 1, 3, 5, and 7 post the injection, respectively. Then, they were weighed and homogenized in sterile PBS (100 mg:0.9 mL). These samples were plated on solid LB agar plates post 1000-fold dilution and cultured at 37  $^{\circ}$ C. After 24 h of incubation, the bacterial colonies on the plates were observed.

### 2.17. In vivo anti-tumor efficacy

#### 2.17.1. Subcutaneous tumor inhibition

When the tumor volume reached  $\sim 80 \text{ mm}^3$ , the mice were randomly divided into four groups and intratumorally injected with 25  $\mu$ L of PBS, *Sal*, *Sal@CaCO<sub>3</sub>*, or *Sal@CaCO<sub>3</sub>/A23187* at a *Sal* dose of  $5 \times 10^6$  CFU per mouse on Days 0, 2 and 6. The tumor volumes were recorded every day. The mice were euthanized on Day 7, with blood collected and major organs (heart, liver, spleen, lung, and kidneys) and tumors dissected for further analysis. The collected tumors were photographed, weighed, and then subjected to hematoxylin and eosin (H&E) and Terminal deoxynucleotidyl

transferase (TdT)-mediated dUTP Nick End Labeling (TUNEL) staining for histological analysis.

### 2.17.2. Tumor metastasis inhibition

When the tumor volume reached  $\sim 50 \text{ mm}^3$ ,  $3.5 \times 10^5$  B16F10-luc cells were intravenously injected into each mouse to establish a pulmonary metastasis model of melanoma (Day -1). The mice were randomly divided into five groups and administrated with PBS, *Sal*, *Sal*@CaCO<sub>3</sub>, *Sal*@CaCO<sub>3</sub>/A23187, or *Sal*@CaCO<sub>3</sub>/A23187+aPD-L1 on Days 0, 2, and 6. The aPD-L1 was injected intraperitoneally at a dose of 7.5 mg/kg, while the others were injected intratumorally at a *Sal* dose of  $5 \times 10^6$  CFU per mouse. The D-Luciferin potassium salt (150 mg/kg) was intraperitoneally injected into the mice on Day 13, followed by euthanizing. The lungs were collected for bioluminescence imaging using the IVIS imaging system (S12-FMT400010, PerkinElmer, Massachusetts, USA) and then photographed. The number of pulmonary metastasis nodules was counted, and H&E staining was performed for histological analysis.

### 2.18. Immunological effects

The immunological effects of *Sal*@CaCO<sub>3</sub>/A23187 were investigated by flow cytometry, WB, immunofluorescence, and ELISA. For flow cytometry, the tumor tissues were ground through 40  $\mu\text{m}$  cell strainers to obtain single cell suspensions and then lysed the red blood cells. The cells were then blocked with CD16/32 blocking reagent, followed by incubating with fluorescence-labeled antibodies for 20 min at 4 °C. For DCs maturation, the cells were stained with anti-CD11c-APC and anti-CD86-PE. For macrophage polarization, the cells were stained with anti-F4/80-PE, anti-CD80-FITC, and anti-CD206-FITC. For T cells activation, the cells were stained with anti-CD3-FITC, anti-CD4-APC, and anti-CD8-PE. The samples were then analyzed by flow cytometry (Beckman Coulter). For WB, the tumor tissues were lysed at 4 °C for 1 h after homogenizing in RIPA lysis buffer (100 mg:1 mL), and the protein samples were collected by centrifugation at 13000 rpm for 15 min (TGL20M, Yingtai, Changsha, China). The WB was performed as described previously with primary antibodies against Cx43, CD80, CD86, CD206, CD4, and CD8. For immunofluorescence, the tumor sections were incubated with the above-mentioned primary antibodies at 4 °C overnight and then stained with secondary antibodies labeled by fluorescence for 1 h, followed by staining cell nuclei with DAPI. These sections were imaged by a fluorescent microscope (Nikon). For ELISA, the tumor tissues were homogenized in ice-cold PBS, and the supernatant was collected after centrifugation at 13000 rpm for 15 min (TGL20M, Yingtai, Changsha, China) to measure the levels of TNF- $\alpha$  and IL-10 by the corresponding ELISA kits.

### 2.19. Safety evaluation

The body weight of mice was recorded every day during the treatments. The major organs were fixed in 4% paraformaldehyde and then performed H&E staining. The blood samples were centrifuged at 3000 rpm for 15 min (TGL20M, Yingtai, Changsha, China) to obtain serum. The serum levels of biochemical indexes, including ALT, AST, BUN, and Cre, were determined by corresponding assay kits. The levels of cytokines, including TNF- $\alpha$ , IFN- $\gamma$ , IL-6, and IL-10, in the serum were determined by corresponding ELISA kits.

### 2.20. Statistical analysis

All the quantitative data were presented as mean  $\pm$  standard deviation (SD). The differences between two groups and among multiple groups were accessed by Student's *t*-test and one-way analysis of variance (ANOVA), respectively, and considered to be statistically significant when  $P < 0.05$  (\* $P < 0.05$ , \*\* $P < 0.01$ , \*\*\* $P < 0.001$ , \*\*\*\* $P < 0.0001$ ).

## 3. Results and discussions

### 3.1. Surface mineralization of *Salmonella* by calcium carbonate with A23187 loading

The surface of *Sal* was coated with the CaCO<sub>3</sub> layer *via in-situ* mineralization by successively adding CaCl<sub>2</sub> and NaHCO<sub>3</sub> into bacteria suspensions, and the resulting *Sal*@CaCO<sub>3</sub> was collected after 5 min reaction. Upon CaCO<sub>3</sub> coating, the morphology of the bacteria was unchanged (Fig. 1A), while the size considerably increased from 1068 nm to 1434 nm (Fig. 1B). The successful CaCO<sub>3</sub> coating could be evidenced by the obvious Ca elemental signal on the *Sal*@CaCO<sub>3</sub> surface (Fig. 1A), and its amount was calculated to be  $\sim 13\%$  based on EDS analysis (Supporting Information Fig. S1). The structure was further confirmed by FT-IR spectra, in which the obtained *Sal*@CaCO<sub>3</sub> showed characteristic peaks of both *Sal* and CaCO<sub>3</sub> (Fig. 1C).

We then adsorbed the calcium ionophore A23187 on the *Sal*@CaCO<sub>3</sub> surface to form *Sal*@CaCO<sub>3</sub>/A23187, and the drug loading could be quantified by the intrinsic fluorescence of A23187 with ultraviolet light irradiation (Supporting Information Fig. S2). Because of the highly hydrophobic nature with low solubility, A23187 pure drug nanoparticles were first prepared (Supporting Information Fig. S3) and then added into *Sal*@CaCO<sub>3</sub> for surface adsorption. At optimal feeding concentration of 100  $\mu\text{M}$  A23187 nanoparticles, loading efficiency achieved  $\sim 24\%$  after 2 h incubation (Supporting Information Fig. S4). Because of the fluorescent nature of A23187, the successful drug loading was further evidenced by both fluorescent photographs and microscopies (Fig. 1D and E).

To figure out whether the surface functionalization had any effects on bacterial viability, we collected bacteria and plated them on LB agar for 24 h incubation. The bacterial colonies were almost the same (Fig. 1F), and the viability was comparable for *Sal*, *Sal*@CaCO<sub>3</sub>, and *Sal*@CaCO<sub>3</sub>/A23187 (Fig. 1G). In addition, we stained the bacteria *via* SYTO9/PI double staining, through which the live bacteria were stained in green while the dead ones were in red (Fig. 1H). From the fluorescence images, no red fluorescence was found for all treatment groups, demonstrating that *Sal* remained alive post the surface decoration. We further monitored the bacterial growth curves, and the same result was observed (Fig. 1I). Collectively, all these experiments demonstrated that the surface mineralization and A23187 loading did not affect the bioactivity of the bacteria.

### 3.2. pH-responsive exfoliation of CaCO<sub>3</sub> shell with co-release of Ca<sup>2+</sup> and A23187 to promote Ca<sup>2+</sup> influx

As biomaterialized material, the most notable property of the CaCO<sub>3</sub> surface is its rapid degradation at the slightly acidic condition that mimics the tumor microenvironment. To study the

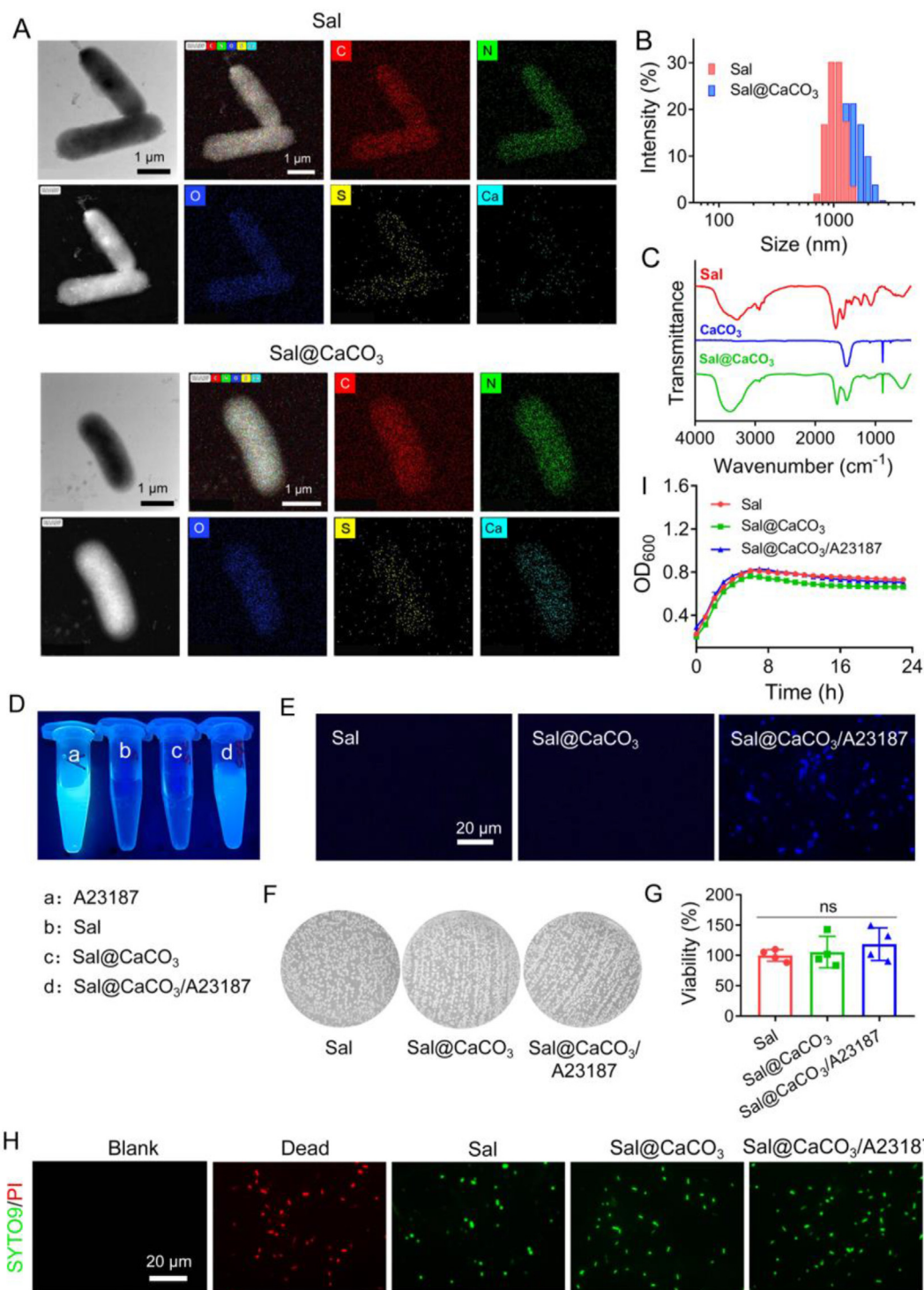


**Figure 1** The characterizations of *Sal*@CaCO<sub>3</sub>/A23187. (A) The TEM images and element mapping of *Sal* and *Sal*@CaCO<sub>3</sub>. Scale bar = 1 μm. (B) The size distribution of *Sal* and *Sal*@CaCO<sub>3</sub>. (C) FT-IR spectra of *Sal*, CaCO<sub>3</sub> and *Sal*@CaCO<sub>3</sub>. (D) The photograph and (E) fluorescent images of various samples taken under ultraviolet light and fluorescent microscope, respectively. Scale bar = 20 μm. (F) The photographs of bacterial colonies of *Sal*, *Sal*@CaCO<sub>3</sub> and *Sal*@CaCO<sub>3</sub>/A23187 after culturing on LB agar for 24 h. (G) The bacterial viability calculated from the number of bacterial colonies in (F). Data are presented as mean ± SD (*n* = 4). ns, not significant. (H) The live/dead bacterial staining by SYTO9/PI double staining. Scale bar = 20 μm. (I) The growth curves of *Sal*, *Sal*@CaCO<sub>3</sub> and *Sal*@CaCO<sub>3</sub>/A23187 by monitoring OD<sub>600</sub> values.

CaCO<sub>3</sub> degradation, Sal@CaCO<sub>3</sub>/A23187 was added into different buffers, and the release of Ca<sup>2+</sup> was measured. Almost no Ca<sup>2+</sup> release was observed at a neutral buffer of pH 7.4, while a rapid and complete Ca<sup>2+</sup> release was seen when lowering the pH to 6.5 (Fig. 2A). This result was consistent with the pH-responsive profile of CaCO<sub>3</sub> reported previously<sup>44</sup>. In line with this, the

release of A23187 was also accelerated (Fig. 2B). Therefore, the pH-responsive degradation of CaCO<sub>3</sub> at acidic pH is beneficial for on-demand drug release at the tumor site. Such pH-responsive CaCO<sub>3</sub> exfoliation was also verified by the FT-IR spectra (Supporting Information Fig. S5) with the disappearance of the characteristic CaCO<sub>3</sub> peaks.

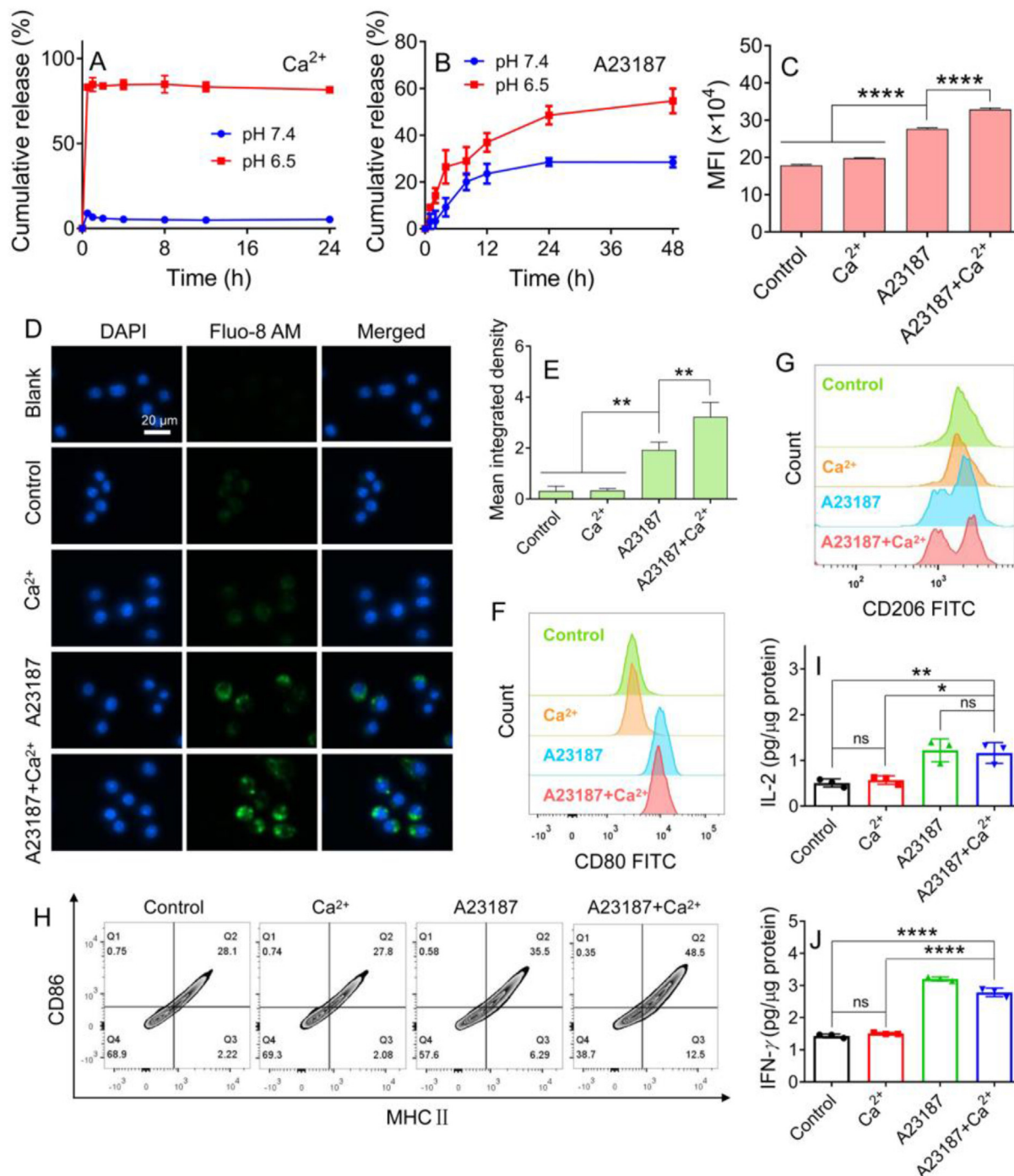


**Figure 2** A23187-mediated Ca<sup>2+</sup> influx and the immunological effects. The cumulative release of (A) Ca<sup>2+</sup> from Sal@CaCO<sub>3</sub> and (B) A23187 from Sal@CaCO<sub>3</sub>/A23187 at pH 7.4/6.5. (C) The intracellular Ca<sup>2+</sup> quantification and (D) the CLSM images of RAW264.7 cells post different treatments after staining with Fluo-8 AM. Scale bar = 20 μm. (E) Quantification results from (D). The flow cytometry results indicating the expression of (F) M1 macrophage marker CD80 and (G) M2 macrophage marker CD206. (H) The quantification of the MHC II and CD86 double positive cells in DC2.4 cells post different treatments by flow cytometry. (I) IL-2 and (J) IFN-γ secretion from Jurkat T cells post different treatments. Data are presented as mean ± SD (n = 3). ns, not significant. \*P < 0.05, \*\*P < 0.01, \*\*\*\*P < 0.0001.

Accompanied by  $\text{CaCO}_3$  degradation, a large amount of  $\text{Ca}^{2+}$  was released at the tumor issue, which can be employed as an ionic messenger to regulate immune responses for better immunotherapy<sup>45</sup>. However,  $\text{Ca}^{2+}$  cannot freely penetrate the hydrophobic lipid layers, which depends on the active transportation mediated by specific membrane proteins such as transporters, pumps, and ion channels<sup>45</sup>. For example, the intracellular  $\text{Ca}^{2+}$  concentration was almost unchanged post the treatment with  $\text{CaCl}_2$  (Fig. 2C), suggesting limited penetration. To this end, A23187, a commonly used calcium ionophore, was co-delivered in this work, which was expected to facilitate intracellular delivery of  $\text{Ca}^{2+}$ . A23187 is a biocompatible ionophore that showed non-toxicity towards immune cells of both RAW264.7 and DC2.4 cells at a concentration below 5  $\mu\text{mol/L}$  (Supporting Information Fig. S6). Notably, A23187 alone could increase the cytosol  $\text{Ca}^{2+}$  concentration (Fig. 2C), which is due to its activity to promote the transportation of intracellular  $\text{Ca}^{2+}$  stores into cytosol<sup>43</sup>. Upon addition of free  $\text{Ca}^{2+}$ , the cytosol  $\text{Ca}^{2+}$  was further increased after 12 h incubation, attributable to the A23187-mediated  $\text{Ca}^{2+}$  influx across the cell membrane. The  $\text{Ca}^{2+}$  influx was also visualized by a fluorescent  $\text{Ca}^{2+}$  probe of Fluo-8 AM (Fig. 2D), and the intensity was quantified in Fig. 2E. Note that although the maximum excitation wavelength and emission wavelength of A23187 and DAPI were close to each other, the signal of A23187 at the concentration we used showed no interference on DAPI visualization (Supporting Information Fig. S7). Compared to the control and  $\text{Ca}^{2+}$  treatment alone, a much stronger fluorescence was observed for the A23187 group, and the A23187 plus  $\text{Ca}^{2+}$  displayed the highest intensity. Therefore, the co-release of A23187 and  $\text{Ca}^{2+}$  could promote the influx of  $\text{Ca}^{2+}$  into immune cells to exert its subsequent biological functions.

Having demonstrated the effective  $\text{Ca}^{2+}$  influx, we next explored its effect on immune regulation. It has been shown that the influx of  $\text{Ca}^{2+}$  could regulate various immune cells, such as reprogramming tumor-associated macrophages, enhancing the antigen presentation of DCs, and activating the function of cytotoxic T lymphocytes<sup>46–48</sup>. To examine this, we investigated the immunological effects of  $\text{Ca}^{2+}$  influx *in vitro*. The RAW264.7 cells were pretreated with IL-4 (100 ng/mL) for M2 polarization, and the expression of CD80 (M1 macrophage marker) and CD206 (M2 macrophage marker) were detected after various treatments (Fig. 2F and G). As expected, the cells treated with A23187 and A23187 plus  $\text{Ca}^{2+}$  showed increased expression of CD80 and decreased expression of CD206, suggesting M2-to-M1 repolarization. Then, the MHC II and CD86 double-positive cells were quantified to assess DCs maturation (Fig. 2H), and the number of matured DCs significantly increased for the A23187 and A23187 plus  $\text{Ca}^{2+}$ . In addition, the secretory levels of IL-2 and IFN- $\gamma$  from Jurkat T cells were significantly increased post the treatment with A23187 and A23187 plus  $\text{Ca}^{2+}$  (Fig. 2I and J), confirming T cells activation. Therefore, A23187-mediated influx of  $\text{Ca}^{2+}$  could systematically regulate immune cells from different aspects, including macrophage repolarization, DCs maturation, as well as T cell activation, all of which are highly important to remodel tumor microenvironment for immunotherapy.

### 3.3. Combinatorial immune activation by *Sal* and $\text{Ca}^{2+}$ influx

With such immune activation capability of  $\text{Ca}^{2+}$  influx, we then studied its combination effect with *Sal*. *Sal* could combat tumors *via* various mechanisms, such as directly damaging tumor cells and inducing anti-tumor immunity<sup>19</sup>. By using B16F10 as a tumor

cell model, free *Sal* could induce  $\sim 99\%$  cell apoptosis at the dose of  $1 \times 10^8$  CFU after 24 h incubation (Fig. 3A). Interestingly, the *Sal*@ $\text{CaCO}_3$  showed a comparable anti-tumor effect, consistent with the above results that  $\text{CaCO}_3$  coating had no influence on the bioactivities of *Sal*. Upon acidic pre-treatment to degrade the  $\text{CaCO}_3$  shell, the anti-tumor effect was also observed. In addition, the cell death pattern was measured by detecting three classic danger-associated molecular patterns (DAMPs), including calreticulin (CRT), high-mobility group box 1 protein (HMGB1), and adenosine triphosphate (ATP). Upon treatment, significantly enhanced CRT exposure was observed on the cell surface, accompanied by the increase in extracellular release of HMGB1 and ATP (Fig. 3B–E). These results demonstrated the capability of *Sal* to induce tumor cells' immunogenic cell death (ICD), which is important for tumor immunotherapy. Similar results were also observed for *Sal*@ $\text{CaCO}_3$ .

Besides directly damaging tumor cells, *Sal* could also promote the crosstalk between tumor cells and DCs *via* the formation of the gap junction for antigen presentation. To demonstrate this, the expression of connexin 43 (Cx43) protein, the main constituent of the gap junction, was measured (Fig. 3F and G). The Cx43 protein was upregulated in both B16F10 and DC2.4 cells post the treatment of *Sal*, and *Sal*@ $\text{CaCO}_3$  at pH 7.4 or 6.5 (to degrade  $\text{CaCO}_3$  shell) exhibited a similar effect. Such up-regulation of the Cx43 protein lays the basis for crosstalk between these two cells. To further probe such an effect, a fluorescent dye was pre-loaded into B16F10 cells, and flow cytometry was employed to monitor the dye transfer (Fig. 3H). As expected, strong fluorescence was observed in receptor DCs after *Sal* or *Sal*@ $\text{CaCO}_3$  treatment. Therefore, the bacteria could promote Cx43 expression to form the gap junction between tumor cells and DCs for better antigen presentation.

Inspired by the native immune stimulation activities of *Sal* and the immune activation effects of  $\text{Ca}^{2+}$  influx, we suspected that *Sal* and  $\text{Ca}^{2+}$  might have combinatorial effects in triggering anti-tumor immunity. To confirm this, we systematically investigated the status of various immune cells post treatments. First, DC2.4 cells were subject to various treatments, and CD86 and MHC II double-positive cells were detected (Fig. 3I and J). The results showed that the expression of CD86 and MHC II were nearly unchanged post the treatment of *Sal* or *Sal*@ $\text{CaCO}_3$  while significantly increased after treatment with *Sal*@ $\text{CaCO}_3$ /A23187, attributable to A23187-mediated  $\text{Ca}^{2+}$  influx. Therefore, *Sal* facilitates tumor antigen delivery while  $\text{Ca}^{2+}$  influx promotes DCs maturation, which works complementarily for antigen presentations. Then, the M2 polarized macrophages were tested (Fig. 3K–N). Interestingly, *Sal* or *Sal*@ $\text{CaCO}_3$  treatment could increase the level of CD86 and decrease the level of CD206 to a similar extent, which was consistent with our previous work that *Sal* could re-polarize M2 macrophages into M1 phenotype<sup>30</sup>. Among them, *Sal*@ $\text{CaCO}_3$ /A23187 showed the best efficacy, indicating a synergistic effect of *Sal* and  $\text{Ca}^{2+}$  for macrophage polarization. Finally, Jurkat T cells were also studied (Fig. 3O). While *Sal* alone cannot directly activate T cells, *Sal*@ $\text{CaCO}_3$ /A23187 stimulated IFN- $\gamma$  secretion by virtue of  $\text{Ca}^{2+}$  influx. Overall, both *Sal* and  $\text{Ca}^{2+}$  could regulate immune cells in different aspects, which achieved a combinatorial effect for anti-tumor immunity.

### 3.4. Therapeutic effect on subcutaneous tumor

To explore the anti-tumor activity of *Sal*@ $\text{CaCO}_3$ /A23187 *in vivo*, a subcutaneous tumor model was developed, and the therapeutic

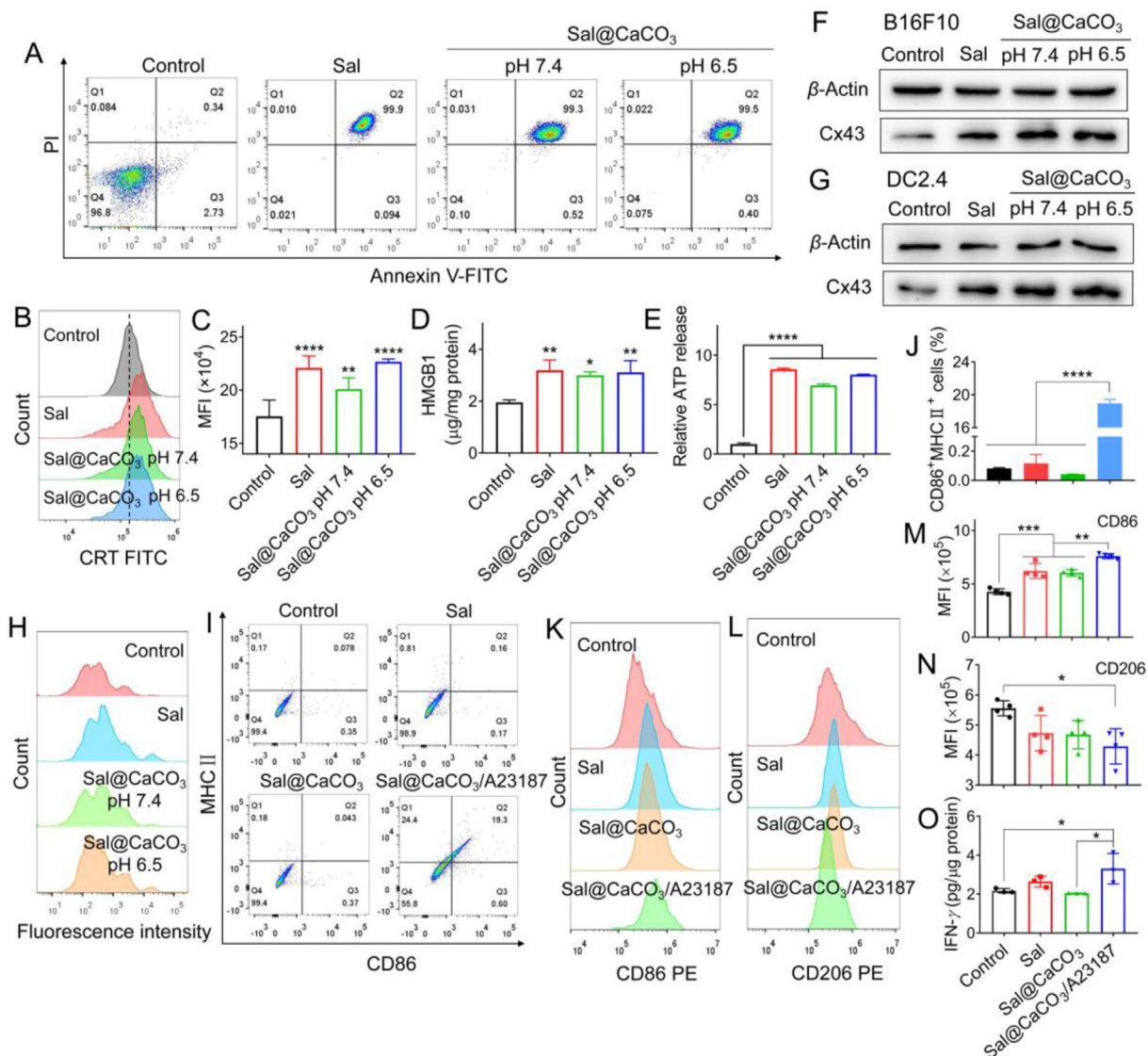


**Figure 3** Combinatorial immunological effects of *Sal* and  $\text{Ca}^{2+}$  influx. (A) The apoptosis of B16F10 cells post different treatments detected by Annexin V-FITC/PI double staining. (B) The flow cytometry results showing the CRT exposure for B16F10 cells post different treatments. (C) The mean fluorescence intensity quantified from (B). The release of (D) HMGB1 and (E) ATP from B16F10 cells post different treatments measured by corresponding kits. The Cx43 expression of (F) B16F10 cells and (G) DC2.4 cells post different treatments. (H) The flow cytometry results indicating the fluorescence intensity of Calcein-AM transferred from B16F10 cells to DC2.4 cells. (I) The analysis of MHC II and CD86 double positive cells in DC2.4 cells post different treatments by flow cytometry. (J) The quantified results from (I). The flow cytometry results indicating the expression of (K) M1 macrophage marker CD86 and (L) M2 macrophage marker CD206. (M,N) The quantified results from (K,L). Data are presented as mean  $\pm$  SD ( $n = 4$ ). (O) IFN- $\gamma$  secretion from Jurkat T cells post different treatments. Data are presented as mean  $\pm$  SD ( $n = 3$ ). \* $P < 0.05$ , \*\* $P < 0.01$ , \*\*\* $P < 0.001$ , \*\*\*\* $P < 0.0001$ .

regime was shown in Fig. 4A. The mice-derived melanoma developed very fast, reaching over 1000  $\text{cm}^3$  within 6 days (Fig. 4B and C). Compared to the PBS control, a moderate tumor growth inhibition was observed for *Sal* owing to its intrinsic anti-tumor activity. After treatment with *Sal@CaCO<sub>3</sub>*, the tumor growth was further delayed, which might be ascribed to the capacity of  $\text{CaCO}_3$  to neutralize the acidic tumor microenvironment and thus attenuate the immunosuppression. By virtue of its capability to modulate the acidity of the tumor microenvironment,  $\text{CaCO}_3$  has been reported to polarize tumor-associated macrophages towards M1 phenotype, increase the infiltration and activity of lymphocytes in the tumor while reducing the inhibitory

regulatory T cells and myeloid-derived suppressor cells<sup>49,50</sup>. To confirm this, *Sal@CaCO<sub>3</sub>* was suspended in an acidic buffer, and we indeed observed a gradual increase of pH value in 30 min (Supporting Information Fig. S8). Obviously, *Sal@CaCO<sub>3</sub>/A23187* achieved the best efficacy, giving significant tumor growth inhibition. To allow direct observation, the tumors were collected for photographing (Fig. 4D) and weighing (Fig. 4E) after treatments, and the tumor slices were further subjected to histological analysis. As expected, the tumor tissue showed a large amount of karyopyknosis and cavitation for the *Sal@CaCO<sub>3</sub>/A23187* treatment group based on H&E staining (Fig. 4F), and the highest apoptosis was detected from TUNEL staining (Fig. 4G).

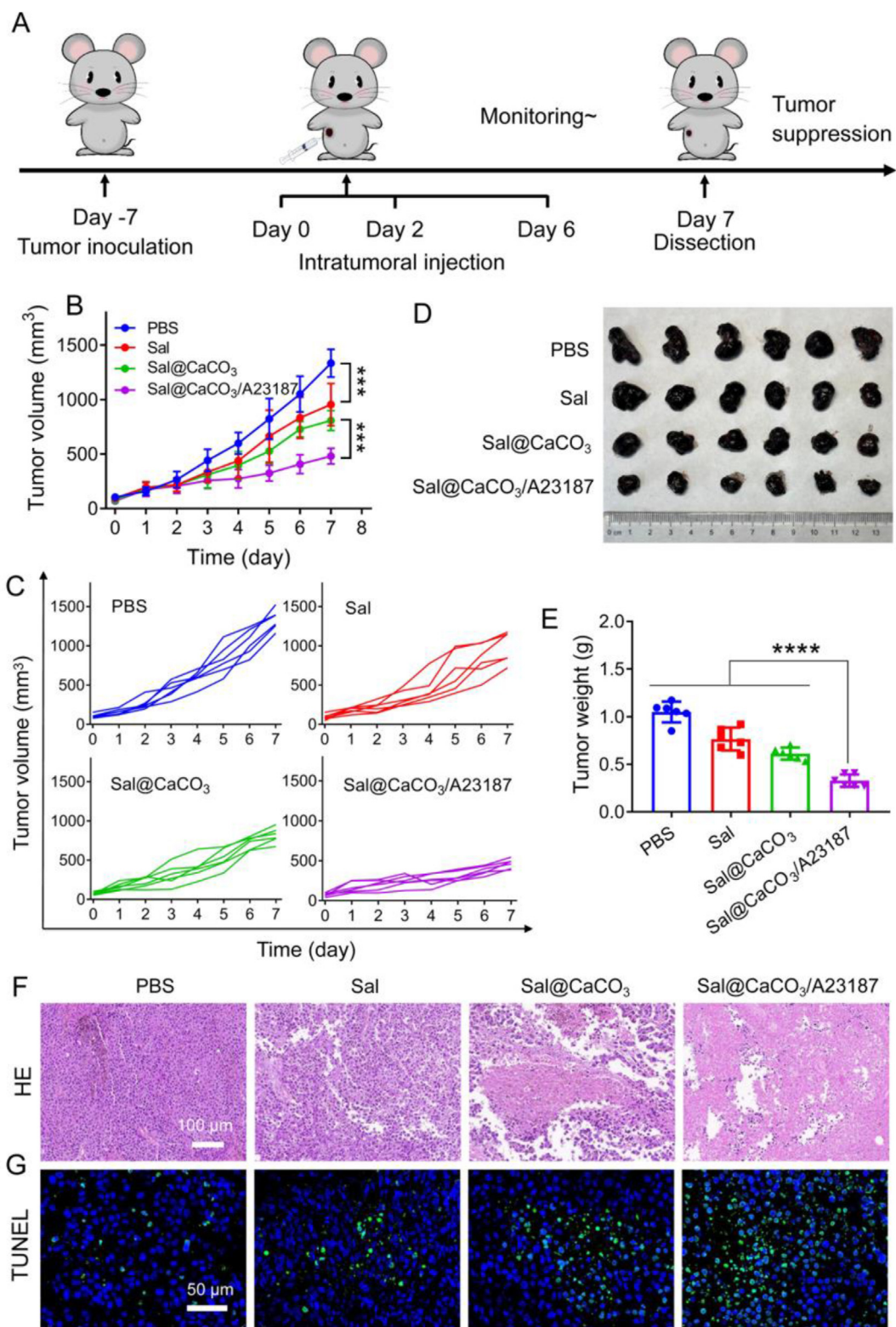


**Figure 4** The anti-tumor effects of *Sal@CaCO<sub>3</sub>/A23187*. (A) Schematic illustration of the therapeutic schedule for subcutaneous tumor inhibition experiment. (B) The tumor growth curves of mice post different treatments. (C) The individual tumor growth curves in different groups. (D) The photographs and (E) weight of tumors harvested from mice post different treatments. Data are presented as mean  $\pm$  SD ( $n = 6$ ). \*\*\* $P < 0.001$ , \*\*\*\* $P < 0.0001$ . (F) The H&E staining images of tumor sections from mice post different treatments. Scale bar = 100  $\mu$ m. (G) The TUNEL staining images of tumor sections from mice post different treatments. Scale bar = 50  $\mu$ m.

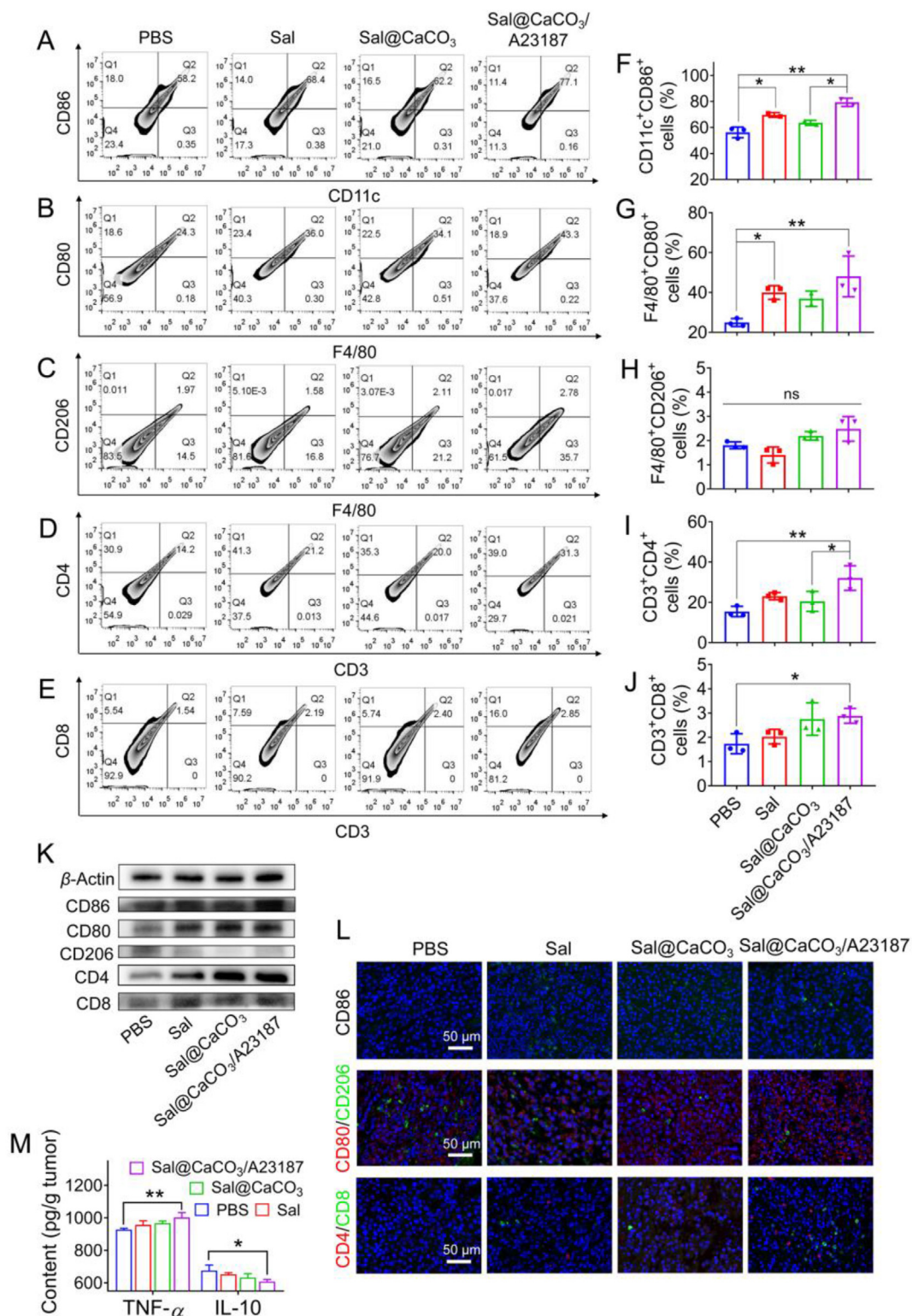


**Figure 5** The anti-tumor mechanisms of *Sal@CaCO<sub>3</sub>/A23187*. The representative flow cytometry results indicating the ratio of (A) activated DCs (CD11c<sup>+</sup>CD86<sup>+</sup>), (B) M1 macrophages (F4/80<sup>+</sup>CD80<sup>+</sup>), (C) M2 macrophages (F4/80<sup>+</sup>CD206<sup>+</sup>), (D) CD4<sup>+</sup> T cells (CD3<sup>+</sup>CD4<sup>+</sup>) and (E) CD8<sup>+</sup> T cells (CD3<sup>+</sup>CD8<sup>+</sup>). (F–J) The quantified results of (A–E). (K) The protein expression of CD86, CD80, CD206, CD4 and CD8 in tumor tissues of mice post different treatments. (L) The immunofluorescence images of CD86, CD80, CD206, CD4 and CD8 in tumor sections from mice post different treatments. Scale bar = 50  $\mu$ m. (M) The content of TNF- $\alpha$  and IL-10 in tumor tissues of mice post different treatments. Data are presented as mean  $\pm$  SD ( $n = 3$ ). ns, not significant. \* $P < 0.05$ , \*\* $P < 0.01$ .

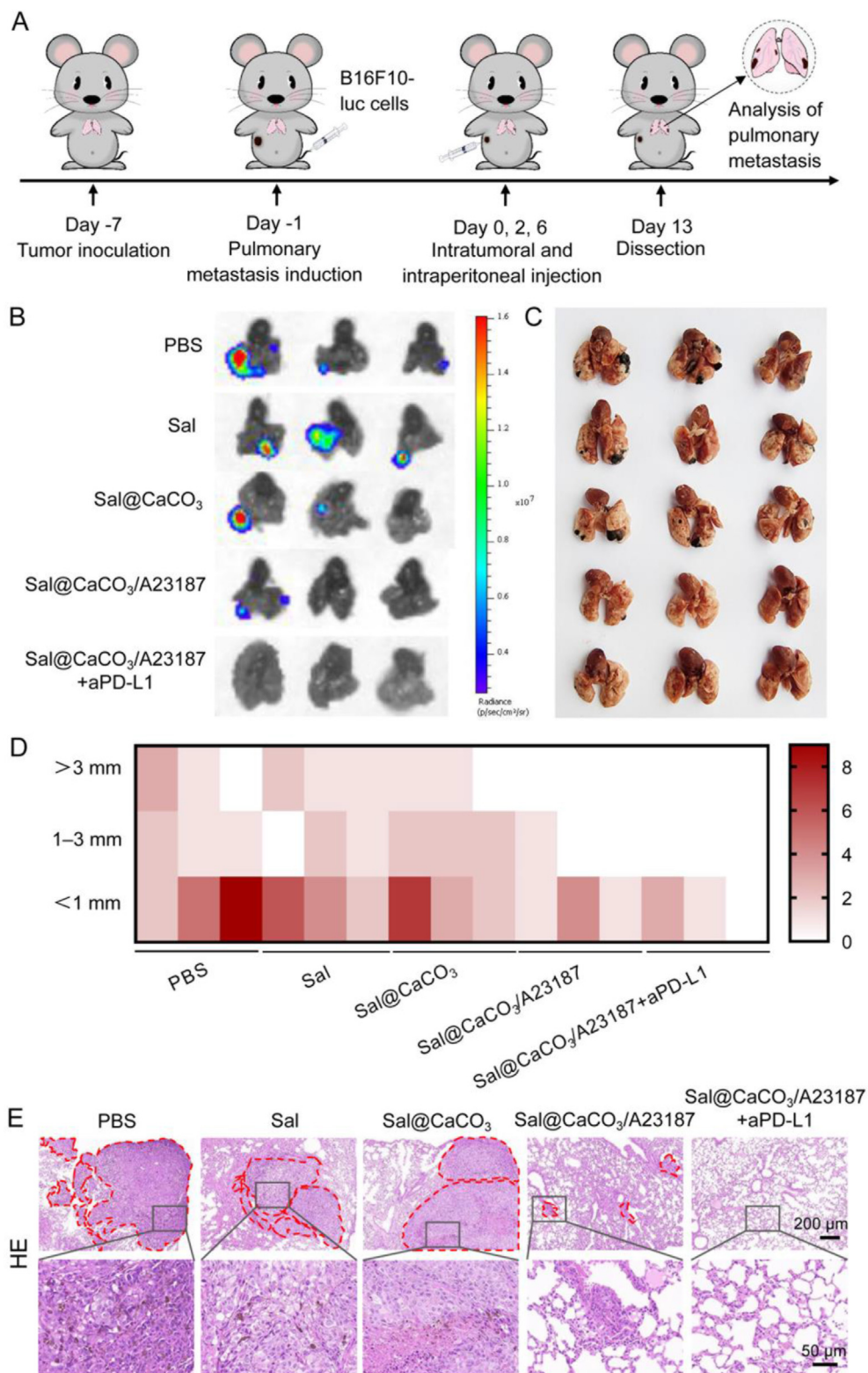


**Figure 6** The anti-metastasis effects of *Sal@CaCO<sub>3</sub>/A23187*. (A) Schematic illustration of the therapeutic schedule for tumor metastasis inhibition experiment. (B) The bioluminescence images and (C) photographs of lungs harvested from mice post different treatments. (D) The heat map showing the number of pulmonary metastatic nodules with various diameters in each group. (E) The H&E staining images of lung sections from mice post different treatments.

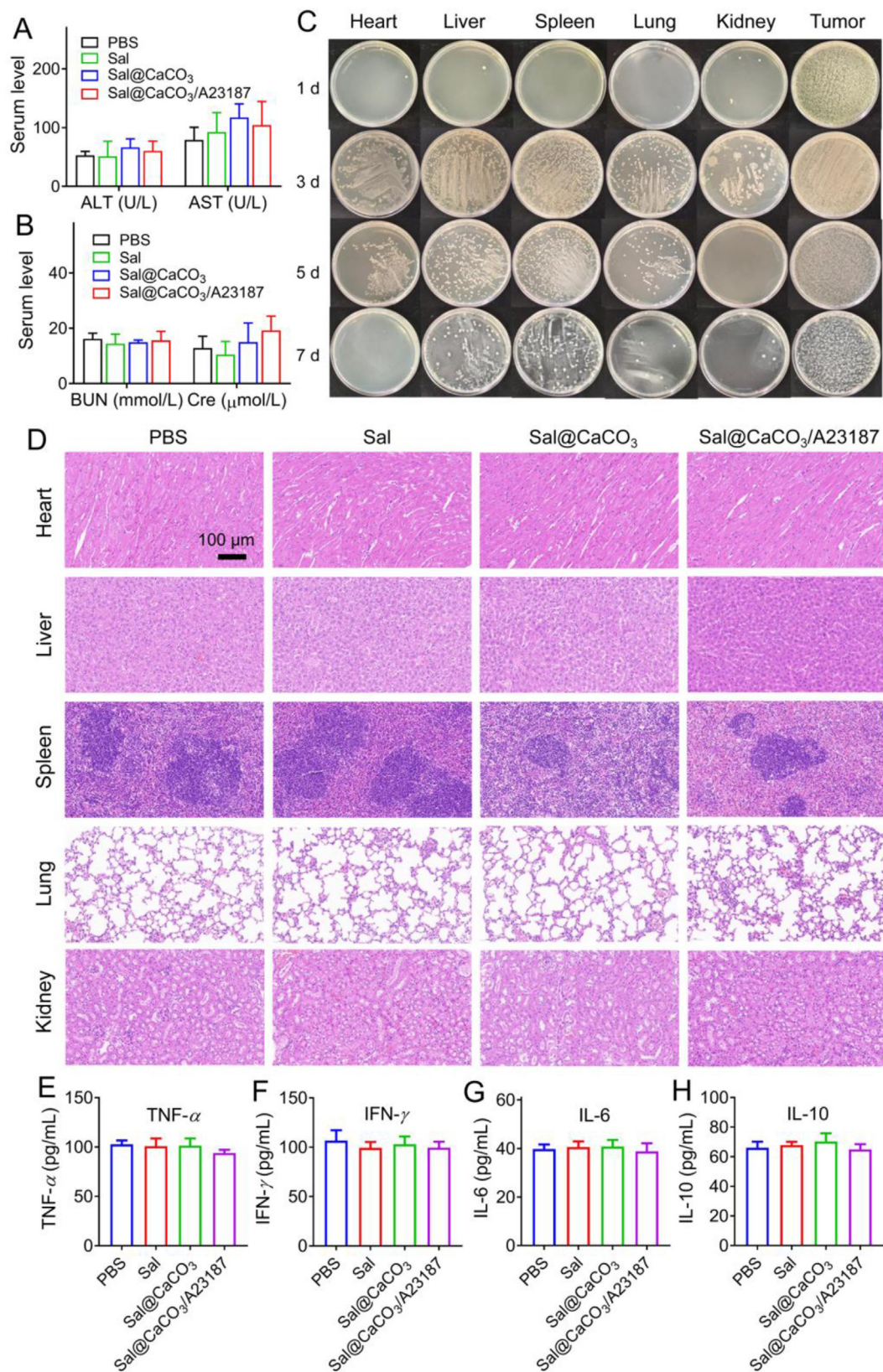


**Figure 7** *In vivo* biosafety of Sal@CaCO<sub>3</sub>/A23187. The serum level of biochemical indexes including (A) ALT, AST and (B) BUN, Cre. (C) The photographs of bacterial colonies after plating the homogenate of various organs and tumors on LB agar and cultured overnight. (D) The H&E staining images of organs from mice post different treatments. Scale bar = 100 μm. The level of (E) TNF-α, (F) IFN-γ, (G) IL-6 and (H) IL-10 in the serum of mice post different treatments. Data are presented as mean ± SD (*n* = 6).

All these results demonstrated the therapeutic efficacy of *Sal*@CaCO<sub>3</sub>/A23187.

### 3.5. The exploration of anti-tumor mechanisms

Encouraged by the anti-tumor efficacy of *Sal*@CaCO<sub>3</sub>/A23187, we then investigated its anti-tumor mechanisms by examining the alteration of tumor immune microenvironment after treatments (Fig. 5). *Sal* treatment promoted DCs activation as evidenced by the increase of CD86 signal (Fig. 5A and F), which can be ascribed to the upregulation of Cx43 to form gap junction between DCs and tumor cells. For the *Sal*@CaCO<sub>3</sub>/A23187, the CD86 signal was even stronger, suggesting a synergistic effect between *Sal* and its CaCO<sub>3</sub> shell. Notably, *Sal*@CaCO<sub>3</sub>/A23187 displayed significantly better efficacy than *Sal*@CaCO<sub>3</sub>, highlighting the necessity of A23187 co-delivery to promote Ca<sup>2+</sup> influx. For macrophages, we also observed a synergistic effect (Fig. 5B and C, 5G and H), in which *Sal*@CaCO<sub>3</sub>/A23187 produced the highest level of F4/80<sup>+</sup>CD80<sup>+</sup> signal (M1 macrophages), while the M2 macrophages (F4/80<sup>+</sup>CD206<sup>+</sup>) did not show significant change. As the final effector cells, CD4<sup>+</sup> T cells (CD3<sup>+</sup>CD4<sup>+</sup>) and CD8<sup>+</sup> T cells (CD3<sup>+</sup>CD8<sup>+</sup>) were also studied (Fig. 5D and E, 5I and J), and as expected, significant activation was observed, especially for *Sal*@CaCO<sub>3</sub>/A23187. In addition, the expression of related proteins, including CD86, CD80, CD206, CD4, and CD8, were measured by Western blot (Fig. 5K) and immunofluorescence (Fig. 5L), and consistent results were observed for all these biomarkers. In line with these, typical cytokines, including tumor necrosis factor- $\alpha$  (TNF- $\alpha$ ) and interleukin-10 (IL-10), were also measured by ELISA (Fig. 5M). TNF- $\alpha$  is the key element of cellular immunity, while IL-10 is a negative regulator of immune responses<sup>51,52</sup>. After treatments, the secretion of TNF- $\alpha$  increased while IL-10 was reduced, further confirming the activation of anti-tumor immunity.

### 3.6. Inhibition of tumor metastasis

Tumor metastasis is the main cause of the death of melanoma patients, which remains a formidable challenge for tumor management. Fortunately, immunotherapy has shown the potential to inhibit tumor metastasis due to the activation of immune responses to damage both primary and distant tumors. Given the systematic immune regulation of *Sal*@CaCO<sub>3</sub>/A23187, we next explored its capability to inhibit tumor metastasis. The lung is the most common metastatic target for melanoma, and we established a pulmonary metastasis model by injecting luciferase-tagged B16F10 cells (B16F10-luc) into mice intravenously. Meanwhile, the subcutaneous tumor was also inoculated to allow intratumoral administration. After the treatments as described in Fig. 6A, the lung of each mouse was collected for various analyses to assess the extent of pulmonary metastasis. Specifically, obvious metastatic nodules in the lung with strong fluorescent signals were observed for the PBS control from both bioluminescence imaging (Fig. 6B) and photographs (Fig. 6C), demonstrating the successful development of the metastatic model. In this case, *Sal* or *Sal*@CaCO<sub>3</sub> treatment failed to show strong therapeutic benefits. For *Sal*@CaCO<sub>3</sub>/A23187 group, by contrast, the diameter of metastasis was much smaller than the control, attributable to its strong immune activation effect. We further combined *Sal*@CaCO<sub>3</sub>/A23187 with PD-L1 antibody (aPD-L1), a widely used immunotherapy of melanoma, and almost complete suppression of tumor metastasis was achieved. For efficacy quantification, the number

of pulmonary metastatic nodules with different diameters was counted (Fig. 6D), which clearly showed the best efficacy of *Sal*@CaCO<sub>3</sub>/A23187 to inhibit metastasis, especially when combined with aPD-L1. To confirm this, the lung tissues were also analyzed by H&E staining (Fig. 6E), where the metastasis areas were highlighted by red dashed lines. Consistently, no lung metastasis site was seen after *Sal*@CaCO<sub>3</sub>/A23187 plus aPD-L1 treatment, further demonstrating the robust efficacy of *Sal*@CaCO<sub>3</sub>/A23187 to control tumor development, migration and invasion.

### 3.7. Safety evaluation

Besides efficacy, another important concern for bacteria-mediated tumor therapy is biosafety, which has attracted great attention. Thus, we systematically evaluated the biocompatibility of *Sal*@CaCO<sub>3</sub>/A23187. The body weight of mice was unchanged during the whole treatment (Supporting Information Fig. S9), and the typical biochemical indexes, including ALT, AST, BUN, and Cre, were within normal ranges (Fig. 7A and B), indicating the lack of acute toxicity. We next studied the biodistribution of the bacteria. To do this, major organs were collected at various time points post the injection, and the bacteria colonization was analyzed by plating on LB agar after homogenization and dilution (Fig. 7C). On Day 1, the bacteria mainly colonized at the tumor site since *Sal*@CaCO<sub>3</sub>/A23187 was administrated *via* intratumoral injection. Interestingly, bacteria were widely distributed on Day 3, indicating the non-specific migration of the live bacteria. As time went on, the number of bacteria in normal organs gradually decreased owing to the immune clearance of the host body. However, a large number of bacteria colonies was still observed at the tumor site over time, which is attributable to the friendly microenvironment of the tumor with rich nutrients and immunosuppression for bacteria growth<sup>32</sup>. Such abundant bacteria colonization in tumors also lays the basis for bacteria-mediated tumor therapy. To confirm the biosafety, the normal organs were collected for H&E staining (Fig. 7D), and no pathological change was observed. In addition, infection-related cytokines, including TNF- $\alpha$ , interferon- $\gamma$  (IFN- $\gamma$ ), IL-6, and IL-10, were also determined in view of the potential risk of bacteria-associated cytokine storm syndrome<sup>53</sup>, while all these tested cytokines showed negligible changes post various treatments (Fig. 7E–H). Collectively, *Sal*@CaCO<sub>3</sub>/A23187 served as a highly biocompatible platform for biological applications.

## 4. Conclusions

In summary, we developed a simple yet effective bacteria-based therapeutic vaccine to realize *in-situ* tumor vaccine generation without the need for auxiliary therapies or stimulations. The *Sal*@CaCO<sub>3</sub>/A23187 was facilely prepared under ambient conditions and carefully characterized, which showed that the biomineralized *Sal* maintained viability, self-reproduction activity, as well as tumoricidal capability. By virtue of its capabilities to induce tumor cells ICD and promote gap junction formation, such biomineralized bacteria could transform primary tumors into a depot of *in-situ* autologous cancer vaccines producer. Compared to traditional vaccines that face problems of complicated vaccine manufacture, strict storage conditions, insufficient delivery, and low patient specificity, such *in-situ* vaccines generator could achieve effective vaccination *via* a simple preparation and administration process. Moreover, Ca<sup>2+</sup> minerals

performed robust immune regulation effects to synergize bacteria by reversing ITM, *e.g.*, DCs maturation, M1 macrophages polarization, and enrichment of cytotoxic T cells. As a result, *Sal*@CaCO<sub>3</sub>/A23187 could effectively suppress both primary and metastatic tumor growth by evoking intratumoral and systemic immune responses, and the efficacy can be further enhanced in combination with ICIs therapy. Finally, the safety of such biomaterialized bacteria has been studied, and *Sal* can be cleared in normal organs without any infection-related side effects while selectively colonized in tumor tissue for consecutive anti-tumor activities. Given the high biocompatibility of CaCO<sub>3</sub> and clinic applications of the *Sal* with satisfactory biosafety, such a bioactive vaccine showed great potential for real clinic translation. Collectively, this work provides a simple and promising strategy for the development of personalized cancer vaccines and paves the way for new applications of bacteria-mediated cancer therapy.

### Acknowledgments

This work was supported by the National Natural Science Foundation of China (No. 82073799), the Natural Science Foundation of Hunan Province in China (2021JJ20084), and the Science and Technology Innovation Program of Hunan Province in China (2021RC3020).

### Author contributions

Lina Guo, Jinsong Ding, and Wenhui Zhou conceived and designed the research. Lina Guo carried out the experiments and performed data analysis. Jinsong Ding and Wenhui Zhou supervised the research. Lina Guo wrote the manuscript. Wenhui Zhou revised the manuscript. All of the authors have read and approved the final manuscript.

### Conflicts of interest

The authors have no conflicts of interest to declare.

### Appendix A. Supporting information

Supporting data to this article can be found online at <https://doi.org/10.1016/j.apsb.2023.08.028>.

### References

1. Tan SZ, Li DP, Zhu X. Cancer immunotherapy: pros, cons and beyond. *Biomed Pharmacother* 2020;**124**:109821.
2. Kennedy LB, Salama AKS. A review of cancer immunotherapy toxicity. *CA Cancer J Clin* 2020;**70**:86–104.
3. Chen FM, Li TL, Zhang HJ, Saeed M, Liu XY, Huang LJ, et al. Acid-ionizable iron nanoadjuvant augments STING activation for personalized vaccination immunotherapy of cancer. *Adv Mater* 2023;**35**:2209910.
4. Zhou L, Hou B, Wang DG, Sun F, Song RD, Shao Q, et al. Engineering polymeric prodrug nanoplatfor for vaccination immunotherapy of cancer. *Nano Lett* 2020;**20**:4393–402.
5. Dai HX, Fan Q, Wang C. Recent applications of immunomodulatory biomaterials for disease immunotherapy. *Explorations* 2022;**2**:20210157.
6. Li TT, Qian CY, Gu Y, Zhang J, Li SW, Xia NS. Current progress in the development of prophylactic and therapeutic vaccines. *Sci China Life Sci* 2023;**66**:679–710.
7. Wu H, Fu XL, Zhai YJ, Gao S, Yang XY, Zhai GX. Development of effective tumor vaccine strategies based on immune response cascade reactions. *Adv Healthcare Mater* 2021;**10**:2100299.
8. Chen FM, Wang YJ, Gao J, Saeed M, Li TL, Wang WQ, et al. Nanobiomaterial-based vaccination immunotherapy of cancer. *Biomaterials* 2021;**270**:120709.
9. Lei L, Huang D, Gao HL, He B, Cao J, Peppas NA. Hydrogel-guided strategies to stimulate an effective immune response for vaccine-based cancer immunotherapy. *Sci Adv* 2022;**8**:eado8738.
10. Liu JH, Guo LN, Mi Z, Liu ZG, Rong PF, Zhou WH. Vascular bursts-mediated tumor accumulation and deep penetration of spherical nucleic acids for synergistic radio-immunotherapy. *J Control Release* 2022;**348**:1050–65.
11. Guo YX, Wang SZ, Zhang XP, Jia HR, Zhu YX, Zhang XD, et al. *In situ* generation of micrometer-sized tumor cell-derived vesicles as autologous cancer vaccines for boosting systemic immune responses. *Nat Commun* 2022;**13**:6534.
12. Yang X, Yang Y, Bian JY, Wei JJ, Wang Z, Zhou ZW, et al. Converting primary tumor towards an *in situ* sting-activating vaccine via a biomimetic nanoplatfor against recurrent and metastatic tumors. *Nano Today* 2021;**38**:101109.
13. Fang L, Zhao ZT, Wang J, Zhang PC, Ding YP, Jiang YY, et al. Engineering autologous tumor cell vaccine to locally mobilize anti-tumor immunity in tumor surgical bed. *Sci Adv* 2020;**6**:eaba4024.
14. Peng SJ, Xiao FF, Chen MW, Gao HL. Tumor-microenvironment-responsive nanomedicine for enhanced cancer immunotherapy. *Adv Sci* 2022;**9**:2103836.
15. Guo J, Liu P, Wei BL, Peng Y, Ding JS, Zhang HL, et al. Reversing the negative effect of adenosine a1 receptor-targeted immunometabolism modulation on melanoma by a co-delivery nanomedicine for self-activation of anti-PD-L1 DNzyme. *Nano Today* 2023;**48**:101722.
16. Zhu JJ, Chang RM, Wei BL, Fu Y, Chen X, Liu H, et al. Photothermal nano-vaccine promoting antigen presentation and dendritic cells infiltration for enhanced immunotherapy of melanoma via transdermal microneedles delivery. *Research* 2022;**2022**:9816272.
17. Liu P, Shi XY, Peng Y, Hu JM, Ding JS, Zhou WH. Anti-PD-L1 DNzyme loaded photothermal Mn<sup>2+</sup>/Fe<sup>3+</sup> hybrid metal-phenolic networks for cyclically amplified tumor ferroptosis-immunotherapy. *Adv Healthcare Mater* 2022;**11**:2102315.
18. Xu YY, Xiong JY, Sun XY, Gao HL. Targeted nanomedicines remodeling immunosuppressive tumor microenvironment for enhanced cancer immunotherapy. *Acta Pharm Sin B* 2022;**12**:4327–47.
19. Guo YX, Chen Y, Liu XQ, Min JJ, Tan WZ, Zheng JH. Targeted cancer immunotherapy with genetically engineered oncolytic *Salmonella typhimurium*. *Cancer Lett* 2020;**469**:102–10.
20. Chen WF, Wang Y, Qin M, Zhang XD, Zhang ZR, Sun X, et al. Bacteria-driven hypoxia targeting for combined biotherapy and photothermal therapy. *ACS Nano* 2018;**12**:5995–6005.
21. Chen WF, Guo ZF, Zhu YN, Qiao N, Zhang ZR, Sun X. Combination of bacterial-photothermal therapy with an anti-PD-1 peptide depot for enhanced immunity against advanced cancer. *Adv Funct Mater* 2020;**30**:1906623.
22. Guo LN, Ding JS, Zhou WH. Harnessing bacteria for tumor therapy: current advances and challenges. *Chin Chem Lett* 2023:108557. Available from: <https://doi.org/10.1016/j.ccl.2023.108557>.
23. Wang L, Cao ZP, Zhang MM, Lin SS, Liu JY. Spatiotemporally controllable distribution of combination therapeutics in solid tumors by dually modified bacteria. *Adv Mater* 2022;**34**:2106669.
24. Guo HY, Cao ZP, Li JJ, Fu ZZ, Lin SS, Wang L, et al. Integrating bacteria with a ternary combination of photosensitizers for monochromatic irradiation-mediated photoacoustic imaging-guided synergistic photothermal therapy. *ACS Nano* 2023;**17**:5059–71.
25. Monaco A, Chilibroste S, Yim L, Chabalgoity JA, Moreno M. Inflammasome activation, NLRP3 engagement and macrophage recruitment to tumor microenvironment are all required for *Salmonella* anti-tumor effect. *Cancer Immunol Immunother* 2022;**71**:2141–50.

26. Liang K, Liu Q, Li P, Luo HY, Wang HJ, Kong QK. Genetically engineered *Salmonella typhimurium*: recent advances in cancer therapy. *Cancer Lett* 2019;**448**:168–81.
27. Saccheri F, Pozzi C, Avogadri F, Barozzi S, Faretta M, Fusi P, et al. Bacteria-induced gap junctions in tumors favor antigen cross-presentation and anti-tumor immunity. *Sci Transl Med* 2010;**2**:44ra57.
28. Chen MC, Pangilinan CR, Lee CH. *Salmonella* breaks tumor immune tolerance by downregulating tumor programmed death-ligand 1 expression. *Cancers* 2020;**12**:57.
29. Liu T, Chopra AK. An enteric pathogen *Salmonella enterica serovar typhimurium* suppresses tumor growth by downregulating CD44(high) and CD4T regulatory (T-reg) cell expression in mice: the critical role of lipopolysaccharide and braun lipoprotein in modulating tumor growth. *Cancer Gene Ther* 2010;**17**:97–108.
30. Mi Z, Yao Q, Qi Y, Zheng JH, Liu JH, Liu ZG, et al. *Salmonella*-mediated blood–brain barrier penetration, tumor homing and tumor microenvironment regulation for enhanced chemo/bacterial glioma therapy. *Acta Pharm Sin B* 2023;**13**:819–33.
31. Liu Y, Zhang MM, Wang XY, Yang FM, Cao ZP, Wang L, et al. Dressing bacteria with a hybrid immunoactive nanosurface to elicit dual anticancer and antiviral immunity. *Adv Mater* 2023;**35**:e2210949.
32. Zhou SB, Gravekamp C, Bermudes D, Liu K. Tumour-targeting bacteria engineered to fight cancer. *Nat Rev Cancer* 2018;**18**:727–43.
33. Toso JF, Gill VJ, Hwu P, Marincola FM, Restifo NP, Schwartzentruber DJ, et al. Phase I study of the intravenous administration of attenuated *Salmonella typhimurium* to patients with metastatic melanoma. *J Clin Oncol* 2002;**20**:142–52.
34. Heimann DM, Rosenberg SA. Continuous intravenous administration of live genetically modified *Salmonella typhimurium* in patients with metastatic melanoma. *J Immunother* 2003;**26**:179–80.
35. Tyrkalska SD, Candel S, Angosto D, Gomez-Abellan V, Martin-Sanchez F, Garcia-Moreno D, et al. Neutrophils mediate *Salmonella typhimurium* clearance through the GBP4 inflammasome-dependent production of prostaglandins. *Nat Commun* 2016;**7**:12077.
36. Wong CO, Gregory S, Hu HX, Chao YF, Sepulveda VE, He YC, et al. Lysosomal degradation is required for sustained phagocytosis of bacteria by macrophages. *Cell Host Microbe* 2017;**21**:719–30.
37. Cao ZP, Cheng SS, Wang XY, Pang Y, Liu JY. Camouflaging bacteria by wrapping with cell membranes. *Nat Commun* 2019;**10**:3452.
38. Liu R, Cao ZP, Wang L, Wang XY, Lin SS, Wu F, et al. Multimodal oncolytic bacteria by coating with tumor cell derived nanoshells. *Nano Today* 2022;**45**:101537.
39. Westphal K, Leschner S, Jablonska J, Loessner H, Weiss S. Containment of tumor-colonizing bacteria by host neutrophils. *Cancer Res* 2008;**68**:2952–60.
40. Mi Z, Guo LN, Liu P, Qi Y, Feng ZC, Liu JH, et al. "Trojan horse" *Salmonella* enabling tumor homing of silver nanoparticles via neutrophil infiltration for synergistic tumor therapy and enhanced biosafety. *Nano Lett* 2021;**21**:414–23.
41. Geng ZM, Wang XY, Wu F, Cao ZP, Liu JY. Biointerface mineralization generates ultraresistant gut microbes as oral biotherapeutics. *Sci Adv* 2023;**9**:eade0997.
42. Bai S, Lan YL, Fu SY, Cheng HW, Lu ZX, Liu G. Connecting calcium-based nanomaterials and cancer: from diagnosis to therapy. *Nano-Micro Lett* 2022;**14**:145.
43. Kao JP, Li G, Auston DA. Practical aspects of measuring intracellular calcium signals with fluorescent indicators. *Methods Cell Biol* 2010;**99**:113–52.
44. Qi C, Lin J, Fu LH, Huang P. Calcium-based biomaterials for diagnosis, treatment, and theranostics. *Chem Soc Rev* 2018;**47**:357–403.
45. Wang CG, Zhang R, Wei XM, Lv MZ, Jiang ZF. Metalloimmunology: the metal ion-controlled immunity. *Adv Immunol* 2020;**145**:187–241.
46. An JY, Zhang KX, Wang BH, Wu SX, Wang YF, Zhang HL, et al. Nanoenabled disruption of multiple barriers in antigen cross-presentation of dendritic cells via calcium interference for enhanced chemo-immunotherapy. *ACS Nano* 2020;**14**:7639–50.
47. Chen DG, Xie J, Fiskesund R, Dong WQ, Liang XY, Lv JD, et al. Chloroquine modulates anti-tumor immune response by resetting tumor-associated macrophages toward M1 phenotype. *Nat Commun* 2018;**9**:873.
48. Kim KD, Bae S, Capece T, Nedelkovska H, De Rubio RG, Smrcka AV, et al. Targeted calcium influx boosts cytotoxic T lymphocyte function in the tumour microenvironment. *Nat Commun* 2017;**8**:15365.
49. Chen Q, Wang C, Zhang XD, Chen GJ, Hu QY, Li HJ, et al. *In situ* sprayed bioresponsive immunotherapeutic gel for post-surgical cancer treatment. *Nat Nanotechnol* 2019;**14**:89–97.
50. Zhu YJ, Yang ZJ, Dong ZL, Gong YM, Hao Y, Tian LL, et al. CaCO<sub>3</sub>-assisted preparation of pH-responsive immune-modulating nanoparticles for augmented chemo-immunotherapy. *Nano-Micro Lett* 2021;**13**:29.
51. Parent MA, Wilhelm LB, Kummer LW, Szaba FM, Mullarky IK, Smiley ST. Gamma interferon, tumor necrosis factor alpha, and nitric oxide synthase 2, key elements of cellular immunity, perform critical protective functions during humoral defense against lethal pulmonary yersinia pestis infection. *Infect Immun* 2006;**74**:3381–6.
52. Neumann C, Scheffold A, Rutz S. Functions and regulation of T cell-derived interleukin-10. *Semin Immunol* 2019;**44**:101344.
53. Tang XD, Ji TT, Dong JR, Feng H, Chen FQ, Chen X, et al. Pathogenesis and treatment of cytokine storm induced by infectious diseases. *Int J Mol Sci* 2021;**22**:13009.